JOURNAL OF BONE AND MINERAL RESEARCH
Volume 24, Number 7, 2009
Published online on February 16, 2009; doi: 10.1359/JBMR.090218

Introduction of a Phe377del Mutation in ANK Creates a Mouse Model for Craniometaphyseal Dysplasia

I-Ping Chen,[1] Chiachien J. Wang,[1] Sara Strecker,[1] Boguslawa Koczon-Jaremko,[1] Adele Boskey,[2]
and Ernst J. Reichenberger[1]

ABSTRACT: Craniometaphyseal dysplasia (CMD) is a monogenic human disorder characterized by thickening of craniofacial bones and flaring metaphyses of long bones. Mutations for autosomal dominant CMD have been identified in the progressive ankylosis gene *ANKH*. Previous studies of *Ank* loss-of-function models, $Ank^{null/null}$ and $Ank^{ank/ank}$ mice, suggest that *Ank* plays a role in the regulation of bone mineralization. However, the mechanism for *Ank* mutations leading to CMD remains unknown. We generated the first knockin (KI) mouse model for CMD expressing a human mutation (Phe377 deletion) in ANK. Homozygous *Ank* knockin mice ($Ank^{KI/KI}$) replicate many typical features of human CMD including hyperostosis of craniofacial bones, massive jawbones, decreased diameters of cranial foramina, obliteration of nasal sinuses, fusion of middle ear bones, and club-shaped femurs. In addition, $Ank^{KI/KI}$ mice have increased serum alkaline phosphatase and TRACP5b, as reported in CMD patients. Biochemical markers of bone formation and bone resorption, N-terminal propeptide of type I procollagen and type I collagen cross-linked C-terminal telopeptide, are significantly increased in $Ank^{KI/KI}$ mice, suggesting increased bone turnover. Interestingly, $Ank^{KI/KI}$ bone marrow–derived macrophage cultures show decreased osteoclastogenesis. Despite the hyperostotic phenotype, bone matrix in $Ank^{KI/KI}$ mice is hypomineralized and less mature, indicating that biomechanical properties of bones may be compromised by the *Ank* mutation. We believe this new mouse model will facilitate studies of skeletal abnormalities in CMD at cellular and molecular levels.
J Bone Miner Res 2009;24:1206–1215. Published online on February 16, 2009; doi: 10.1359/JBMR.090218

Key words: craniometaphyseal dysplasia, Ank, skeletal phenotype, genetic disorder, biochemical marker

Address correspondence to: *Ernst Reichenberger, PhD, University of Connecticut Health Center (UCHC), Center for Restorative Medicine and Skeletal Development, Department of Reconstructive Sciences, 263 Farmington Avenue, Farmington, CT 06030-3705, USA, E-mail: reichenberger@uchc.edu*

INTRODUCTION

Craniometaphyseal dysplasia (CMD) is characterized by progressive thickening of craniofacial bones and flaring metaphyses with increased radiolucency of long bones. CMD can be diagnosed early in infants and progresses throughout life.(1,2) Hyperostosis of skulls frequently leads to obstruction of cranial nerve foramina. The common consequences of neuronal compression in CMD patients are hearing loss, visual impairment, and facial palsy. Treatment of severe cases of CMD is limited to surgical intervention to decompress obstructed foramina and to correct craniofacial structures. Treatment with calcitonin, which inhibits bone turnover, can correct biochemical abnormalities but has no effect on cranial hyperostosis.(3,4) Calcitriol, a stimulator of bone resorption, in combination with low calcium diet, can improve facial paralysis but has no effect on abnormal metaphyses.(5)

Knowledge of CMD pathoetiology is based on a few case reports, because there has been no animal model available. Previous studies showed normal or decreased serum calcium and phosphorus levels, normal to slightly elevated PTH, and increased serum alkaline phosphatase (ALP), and TRACP in CMD patients.(3,6–9) Histopathological studies of CMD patients showed either increased osteoblast numbers, no osteoclasts in periosteal or endosteal layers, or increased osteoblast and osteoclast numbers.(3,5,10–12) One paper showed decreased osteoclastogenesis in in vitro osteoclast-like cultures derived from bone marrow of a CMD patient.(13) Altogether, these findings are inconsistent and thus the precise pathophysiology of CMD remains obscure.

CMD occurs sporadically or is transmitted as an autosomal dominant (AD) or autosomal recessive (AR) trait. AD CMD is more common and less severe than the AR form.(14) Mutations for AD CMD have been identified in the human *ANK* gene (*ANKH*) in form of point mutations—one amino acid insertions or deletions that cluster mostly in cytoplasmic domains close to the C terminus.(15,16) Mutations in the N terminus of *ANKH* result in another human skeletal disorder, familial calcium pyrophosphate dihydrate deposition disease (CPPDD), characterized by calcification of cartilage and periarticular tissues caused by deposition of CPPD crystals.(17–19)

The authors state that they have no conflicts of interest.

---

[1] Department of Reconstructive Sciences, School of Dental Medicine, University of Connecticut Health Center, Farmington, Connecticut, USA; [2] Hospital for Special Surgery, New York, New York, USA.

Unlike in CMD, CPPDD patients have no apparent defect in skulls or long bones.

Ank is a 492 amino acid protein with 10 or 12 transmembrane domains and is present on plasma membranes, endoplasmic reticulum, Golgi, and mitochondria.(20,21) A highly conserved sequence within vertebrates and its wide expression in skeletal and nonskeletal tissues suggest an important function of Ank.(16,20) Two *Ank* loss-of-function models, *Ank*$^{\mathrm{ank/ank}}$ and *Ank*$^{\mathrm{null/null}}$ mice, share a remarkable similarity in joint and skeletal phenotypes.(22) *Ank*$^{\mathrm{ank/ank}}$ mice carry a premature stop codon in the C terminus and show progressive arthritic destruction of joints with increased hydroxyapatite (HA) deposition, which eventually leads to joint fusions.(23,24) ANK serves as a PPi transporter to channel intracellular PPi to extracellular matrix, thus regulating mineralization in bones and preventing ectopic calcification.(20) Fibroblasts from *Ank*$^{\mathrm{ank/ank}}$ mice show a decrease in extracellular pyrophosphate (ePPi) levels and an increase in intracellular PPi (iPPi) levels compared with wildtype cells.(20)

Although *Ank*$^{\mathrm{null/null}}$ mice develop cranial hyperostosis and narrowing of foramen magnum, several human CMD characteristics such as hyperostotic mandibles, obstruction of nasal sinuses, and flaring metaphyses of femurs are not replicated in these mice.(25) To gain insights into the pathogenesis of craniometaphyseal dysplasia (CMD), we generated a knockin (KI) mouse model expressing one of the most common mutations identified in the AD form of CMD, an in-frame deletion of phenylalanine 377 (Phe377del) in ANK. Our skeletal and biochemical analyses show that *Ank* knockin mice display many CMD-like features and are therefore a useful model for CMD.

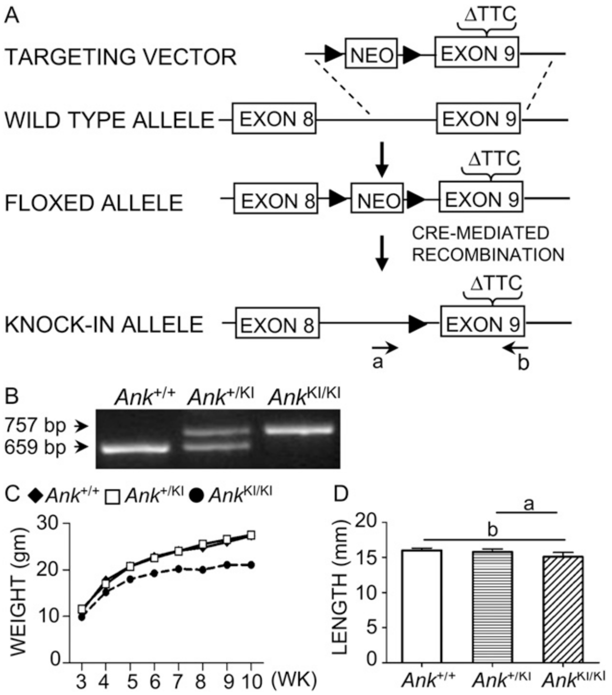

FIG. 1. Generation and genotyping of *Ank*$^{\mathrm{KI/KI}}$ mice. (A) Deletion of phenylalanine 377 in exon 9 introduced into the mouse *Ank* gene by homologous recombination. The floxed allele contains a PGK-Neo cassette (loxP indicated by solid triangle) and a $\mathrm{TTC}_{1130\text{–}1132}$ deletion in exon 9. The knockin allele after cre-mediated recombination contains one loxP site upstream of mutant exon 9. Genotyping primers (a and b) flank the loxP and the deletion site. (B) PCR genotyping assay for *Ank*$^{+/+}$, *Ank*$^{+/\mathrm{KI}}$, and *Ank*$^{\mathrm{KI/KI}}$ animals. Wildtype allele: 659 bp, mutant allele: 757 bp. (C) Total body weight measurement of *Ank*$^{+/+}$, *Ank*$^{+/\mathrm{KI}}$, and *Ank*$^{\mathrm{KI/KI}}$ male mice at 3–10 wk of age ($n \geq 6$). (D) Femur length of 10-wk-old *Ank*$^{+/+}$ ($n = 12$), *Ank*$^{+/\mathrm{KI}}$ ($n = 11$), and *Ank*$^{\mathrm{KI/KI}}$ ($n = 9$) male mice; $^{a}p < 0.05$ and $^{b}p < 0.01$ indicate statistical significance by one-way ANOVA.

MATERIALS AND METHODS

Mice

We generated a knockin mouse model in the Gene Targeting and Transgenic Facility (GTTF) at UCHC introducing a deletion of $\mathrm{TTC}_{1130\text{–}1132}$ (phenylalanine 377) into exon 9 of *Ank*. The TTC deletion was created in a fragment of BAC RP23–296N12 (CHORI, Oakland, CA, USA), which was retrieved in a PL253 vector according to established protocols (http://recombineering.ncifcrf.gov/) and consisted of a 7.1-kb 5′-arm and a 3.2-kb fragment extending 3′ of the mutation. A floxed PGK-Neo cassette was inserted 608 bp 5′ of the TTC deletion. The construct was introduced into 129/Sv embryonic stem cells through recombineering (Fig. 1A). Founder mice were crossed with HPRT1-Cre deleter mice to eliminate a floxed neomycin sequence used for selection of ES cells. Transmission of the mutant allele was confirmed by sequencing. PCR genotyping with tail DNA generates a 659-bp product for wildtype and a 757-bp product for mutant *Ank* (Fig. 1B). The forward primer (5′-GCTAAGCTTCCATACTTACCCGTCTGC-3′) is located 5′ of the remaining loxP site, and the reverse primer (5′-CCTGCCCCTTACCTGGCACTG-3′) is located 3′ of the TTC deletion. In knockin mice, the integrity of the intron preceding exon 9 is maintained except for the presence of a 101-bp fragment containing the remaining loxP site and a short fragment from a multiple cloning site. The animal protocol was approved by the Animal Care Committee of the University of Connecticut Health Center, and all work was performed in an AAALAC-accredited facility under veterinary supervision. Mice were bred from a 129/Sv into a C57Bl/J6 background (N5) for skeletal analysis. *Ank*$^{\mathrm{ank/ank}}$ mice used for skeletal analyses were in C3F3B6A/Aw-J background (Jackson Laboratories).

Skeletal analysis

Radiographs of skulls, mandibles, and femurs of *Ank*$^{+/+}$, *Ank*$^{+/\mathrm{KI}}$, and *Ank*$^{\mathrm{KI/KI}}$ male mice at 1, 3, and 6 mo of age ($n > 3$ for each group) were obtained by a MX20 Radiography System (Faxitron X-ray). BMC and BMD of skulls, mandibles, and femurs from 10-wk-old *Ank*$^{+/+}$ ($n \geq 8$) and *Ank*$^{\mathrm{KI/KI}}$ ($n \geq 6$) mice were determined by DXA using a Lunar PIXImus densitometer (Lunar). Skulls, mandibles, and femurs from 3-mo-old *Ank*$^{+/+}$ ($n = 5$) and *Ank*$^{\mathrm{KI/KI}}$ ($n = 7$) male mice were analyzed using μCT in the MicroCT facility at UCHC (mCT20; ScanCo Medical, Bassersdorf, Switzerland). We also examined *Ank*$^{\mathrm{ank/ank}}$ mice ($n = 5$)

and their wildtype littermates (n = 5). Calvariae were analyzed over an area of 100 slices using the sagittal suture of the central parietal region as reference point. Mandibular data were collected by measuring vertical sections at the mandibular foramen. Trabecular measurements of femurs were taken at the distal growth plate in 80 consecutive slices of 12-μm resolution over a distance of 960 μm. Volumetric regions were rendered as 3D arrays with an isometric voxel dimension of 12 μm. Fifty cross-sectional slices of 12 μm in the mid-diaphysis were used to calculate cortical bone parameters.

Biochemical analysis

Sera were prepared from 10-wk-old fasted $Ank^{+/+}$ ($n \geq 6$) and $Ank^{\mathrm{KI/KI}}$ ($n \geq 7$) male mice. Serum TRACP5b (TRACP5b ELISA kit; IDS), type I collagen cross-linked C-terminal telopeptide (CTX; Ratlaps ELISA kit; Nordic Bioscience), and propeptide of type I procollagen (P1NP; rat/mouse P1NP kit; IDS) were measured according to the manufacturers' instructions. ALP activity was determined directly from serum by a colorimetric method using p-nitrophenol phosphate, which is hydrolyzed by ALP into p-nitrophenol.(26) Briefly, 15 μl of serum was added to substrate solution containing 15 mM 4-nitrophenyl phosphate in 1 M diethanolamine and 0.5 mM $MgCl_2$ (pH 9.8). Absorbance was read at 405 nm after a 5-min incubation.

Bone histomorphometry

We injected $Ank^{+/+}$ (n = 8) and $Ank^{\mathrm{KI/KI}}$ (n = 10) male mice intraperitoneally with calcein (10 mg/kg body weight) and xylenol orange (90 mg/kg body weight) at an interval of 7 days. Two days after the second injection, mice were killed at 10 wk of age, and bones were subjected to histomorphometry as described.(27) For static histomorphometry, calvariae and femurs were fixed in 4% PFA and decalcified in 14% EDTA. Series of 5-μm paraffin sections were stained for TRACP. Osteoblast and osteoclast numbers in an area between 400 and 2,000 μm distal to the growth plate–metaphyseal junction of the distal femur were counted and normalized to the trabecular bone surface. For dynamic histomorphometry, frozen tissues in OCT (Richard-Allan Scientific) were sectioned with a cryotome (CM3050S; Leica). Measurements were obtained by BIOQUANT (BIOQUANT Image Analysis) and OsteoMeasure software (OsteoMetrics) for static and dynamic histomorphometry.

Ash weight

Femurs from 10-wk-old $Ank^{+/+}$ (n = 11) and $Ank^{\mathrm{KI/KI}}$ (n = 11) male mice had been defleshed by Dermestid beetles. Metaphyseal regions and trabeculae were removed from diaphyseal segments. Cortical bones were dried at 105–110°C for 15–17 h, dry weight was measured, and bones were ashed at 600°C for 18–20 h. Mineral content was calculated as the ratio of ash weight to dry weight.

Fourier-transform infrared spectroscopy

Femurs from 10-wk-old $Ank^{+/+}$ (n = 4) and $Ank^{\mathrm{KI/KI}}$ (n = 6) male mice were embedded in polymethyl methacrylate (PMMA). Three-micrometer longitudinal sections were mounted on barium fluoride (BaF_2) infrared windows (Spectral Systems) and examined by Fourier-transform infrared (FTIR) microspectroscopy and imaging using a PerkinElmer Spotlight Imaging System (Perkin Elmer Instruments). A 400 × 400-μm area of cortical bone at the proximal metaphysis was scanned with 6.25 μm spatial resolution, 4 cm^{-1} spectral resolution, and 16 scans/pixel. All spectra were baseline-corrected, and the background spectrum contribution of PMMA was subtracted and processed by ISYS Chemical Imaging Software (v5.0; Spectral Dimensions). The mineral-to-matrix ratio was calculated by the ratio of the integrated area under the phosphate (916–1180 cm^{-1}) and amide I bands (1585–1720 cm^{-1}). Collagen cross-linking was calculated from the intensity ratio of sub-bands at 1660 and 1690 cm^{-1}. Carbonate to phosphate ratio was calculated as area ratio of carbonate (840–900 cm^{-1}) and phosphate bands (916–1180 cm^{-1}). Mineral crystallinity was calculated from the intensity ratio of 1030/1020 cm^{-1}. Data were collected from the center cortex of femurs.

X-ray diffraction

Tibia and scapulae were cleaned of adherent tissues and stored at −20°C before analysis. They were ground in a liquid nitrogen cooled mill (Spex Industries) and subjected to wide-angle X-ray diffraction on a Bruker AX8 diffractometer with Ni-filtered CuK α radiation. Scans were run from 4° 2 θ to 50° 2 theta. The particle size in the c-axis direction was estimated by line-broadening analysis of the 002 peak (25.85° 2 θ) using instrument-provided software. The full width at half-maximum is linearly related to the crystallite size and perfection (t) based on the Debye Scherrer equation.

In vitro osteoclast assays

We used mouse bone marrow–derived macrophage cultures (BMMs) to examine osteoclast formation and function. Briefly, bone marrow was flushed out from femora and tibia of 7- to 9-wk-old mice. Cells were cultured for 18–24 h in αMEM containing 10% FBS (Hyclone), 100 IU/ml penicillin, and 100 μg/ml streptomycin (Gibco Invitrogen). Nonadherent cells were collected and purified by Ficoll separation (Lymphoprep; Axis Shield, Oslo, Norway). Cells were seeded at a density of 5000 cells/well on 96-well culture plates in αMEM with 10% FBS, murine macrophage colony-stimulating factor (mM-CSF; 30 ng/ml; R&D Systems), and mRANKL (30 ng/ml; R&D System) to stimulate osteoclast differentiation. At indicated time points, cells were fixed with 2.5% glutaraldehyde and stained with TRACP (Lymphocyte Acid Phosphatase Kit; Sigma). The $TRACP^+$ cells (nuclei ≥ 3) were counted as mature osteoclasts. For resorption assays, BMMs were cultured for 12 days on calcium phosphate–coated slides (Osteologic Discs; BD Biosciences) and bone chips. Osteologic discs were von Kossa stained and photographed under a dissecting microscope. Resorption pits appear white, contrasting to the black background of remaining mineral. To analyze the resorption pit on bone chips, 12 images for each bone chip were taken using a scanning

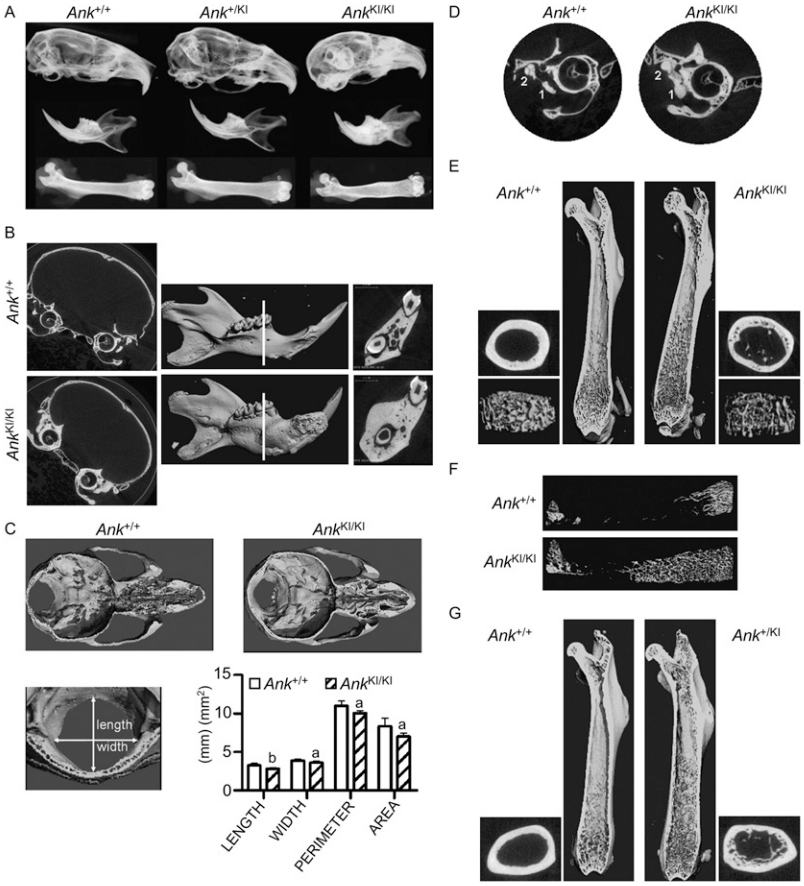

FIG. 2. CMD-like phenotype in $Ank^{KI/KI}$ mice. (A) Representative radiographs of skulls, mandibles, and femurs from 6-mo-old $Ank^{+/+}$, $Ank^{+/KI}$, and $Ank^{KI/KI}$ male mice. (B) μCT images of frontal plane through skulls and 3D reconstruction of mandibles from 3-mo-old $Ank^{+/+}$ and $Ank^{KI/KI}$ male mice. White line indicates sagittal plane through furcation of first mandibular molar. (C) Internal, dorsal view of cranial floor and nasal cavities from horizontal plane of superior semicircular duct and the cribriform plate of ethmoid. Histogram shows dimensions of foramen magnum of $Ank^{+/+}$ and $Ank^{KI/KI}$ littermates. (D) 2D μCT images of tympanic bulla from frontal plane through cochlea showing fusion of malleus (1) and incus (2). (E) Internal view of $Ank^{+/+}$ and $Ank^{KI/KI}$ femurs. 3D reconstructions of trabeculation in metaphysis and cross-sectional slices of cortical bone in diaphysis. (F) 3D μCT images of total trabecular bone in femurs from $Ank^{+/+}$ and $Ank^{KI/KI}$ mice at 10 wk of age. (G) Internal view of femurs of 12-mo-old $Ank^{+/+}$ and $Ank^{+/KI}$ mice. 3D reconstructions of trabeculation in metaphysis and cross-sectional slices of cortical bone in diaphysis.

electronic microscope (TM-1000 Tabletop Microscope; Hitachi High Technologies America). Percent resorption was calculated as the ratio of resorbed area to total area using Adobe Photoshop software for osteologic discs and Digimizer software for bone chips.

Statistical analysis

Statistical analysis was performed by Student's *t*-test or one-way ANOVA as indicated, using Prism 5 software (GraphPad Software).

RESULTS

General appearance of $Ank^{KI/KI}$ mice

$Ank^{KI/KI}$ mice appeared normal at birth but developed stiffness of joints at age of 4–5 wk. Similar to $Ank^{ank/ank}$ and $Ank^{null/null}$ mice, they died around 6 mo of age from an unknown cause. After weaning, $Ank^{KI/KI}$ mice weighed less and had shorter body length than their respective wildtype and heterozygous littermates (Fig. 1C, data not shown). A small but significant decrease in femur length of $Ank^{KI/KI}$ mice was observed at the age of 10 wk (Fig. 1D).

CMD-like skeletal phenotype of $Ank^{KI/KI}$ mice

Diagnosis of CMD in humans is based on clinical and radiographic findings.(11,28) We examined skeletal elements of 1-, 3-, and 6-mo-old $Ank^{+/+}$, $Ank^{+/KI}$, and $Ank^{KI/KI}$ male mice by X-ray imaging. As in CMD patients, $Ank^{KI/KI}$ mice showed increased radiopacity of skulls and mandibles (Fig. 2A). In addition, they exhibited club-shaped femurs with increased radiolucency in metaphyses at all ages examined. In $Ank^{KI/KI}$ mice, this CMD-like phenotype appeared early and progressed with age. $Ank^{+/KI}$ mice were phenotypically normal but developed an intermediate phenotype as they aged. This observation suggests that the effect of the *Ank* mutation may be dose and time dependent.

We examined BMC and BMD of $Ank^{+/+}$ and $Ank^{KI/KI}$ mice by DXA. Our results showed that $Ank^{KI/KI}$ mice had increased BMC and BMD in skulls and mandibles, whereas measurements of cortical bones in diaphyses showed increased BMC but normal BMD (Table 1). The same cortical diaphyses were subjected to ash weight determination. Unexpectedly, ash content in the $Ank^{KI/KI}$ group (67.487 ± 1.255%, $n = 11$) was significantly lower compared with $Ank^{+/+}$ mice (69.731 ± 1.398%, $n = 11$; $p < 0.01$). This finding was consistent with μCT, which showed a 5% reduction of cortical tissue density in $Ank^{KI/KI}$ mice (Table 2).

To better characterize the bone phenotype, we studied the skeleton of 3-mo-old $Ank^{+/+}$ and $Ank^{KI/KI}$ mice by μCT. Craniofacial bones of $Ank^{KI/KI}$ mice displayed hyperostosis, especially in the cranial base and the mandibles (Fig. 2B). $Ank^{KI/KI}$ mice showed a trend for increase in

TABLE 1. DXA Measurement of $Ank^{+/+}$ and $Ank^{KI/KI}$ Mice

	$Ank^{+/+}$			$Ank^{KI/KI}$		
	Skull (n = 8)	*Mandible (n = 8)*	*Femur (n = 11)*	*Skull (n = 6)*	*Mandible (n = 6)*	*Femur (n = 11)*
BMC (g)	0.176 ± 0.011	0.028 ± 0.002	0.008 ± 0.002	0.251 ± 0.008*	0.039 ± 0.004*	0.011 ± 0.001†
BMD (g/cm^2)	0.087 ± 0.004	0.063 ± 0.002	0.058 ± 0.007	0.123 ± 0.003*	0.078 ± 0.005*	0.060 ± 0.003

Measurements of mice at 10 wk of age were determined by DXA. Data are mean ± SD for groups of 6–11 mice.

* $p < 0.01$.

† $p < 0.05$.

TABLE 2. μCT Analysis of 3-mo-old $Ank^{+/+}$ and $Ank^{KI/KI}$ Male Mice

	$Ank^{+/+}$ *(n = 5)*	$Ank^{KI/KI}$ *(n = 7)*
Calvariae		
Cortical width (mm)	0.14 ± 0.02	0.17 ± 0.01*
BM/TA (%)	16.9 ± 2.2	16.1 ± 7.3
BA/TA (%)	83.1 ± 2.2	83.9 ± 7.3
Mandibles		
BVF (%)	77 ± 1.9	88.7 ± 2.8†
Dentin density	1493 ± 62	1311 ± 106†
Femurs trabecular bone (metaphyses)		
BVF (%)	30.2 ± 7.1	10.7 ± 1.4†
Trabecular number(N/mm)	5.94 ± 0.48	5.02 ± 0.38†
Trabecular thickness (μm)	66 ± 14	45 ± 5†
Trabecular spacing (μm)	160 ± 20	196 ± 17‡
Femurs cortical bone (diaphyses)		
Subperiosteal area (mm^2)	1.94 ± 0.241	2.35 ± 0.29‡
Subendosteal area (mm^2)	0.79 ± 0.14	1.22 ± 0.18†
Cortical porosity (%)	3.4 ± 0.6	5.7 ± 2.1†
Tissue density (mg/cm^3 HA)	1502 ± 19	1435 ± 18†
Femurs whole trabecular bone		
Bone volume (mm^3)	1.005 ± 0.22	1.280 ± 0.33
SMI	1.8 ± 0.4	2.9 ± 0.3†

BM, calvarial total bone marrow space; BA, calvarial bone area; TA, calvarial total area; BV, bone volume; TV, total volume; BVF, BV/TV.

Data are mean ± SD.

* $p = 0.0505$ for cortical width.

† $p < 0.01$.

‡ $p < 0.05$.

calvarial width ($p = 0.0505$) and a significant increase in bone mass of mandibles (Table 2). Hyperostosis of the cranial base in $Ank^{KI/KI}$ mice was accompanied by narrowing of cranial neural foramina and obliteration of nasal sinuses (Fig. 2C). The size of the foramen magnum was significantly reduced in all dimensions (Fig. 2C). Moreover, 2D images showed fusion of incus and malleus in $Ank^{KI/KI}$ mice, suggesting impaired hearing (Fig. 2D). Another characteristic of CMD patients is flaring metaphysis with increased radiolucency. $Ank^{KI/KI}$ mice exhibited abnormal shape of femurs with increased diameter of cortical bone and undertrabeculated metaphyses (Fig. 2E; Table 2). These metaphyseal trabeculae were reduced, both in thickness and numbers, compared with $Ank^{+/+}$ mice. Furthermore, $Ank^{KI/KI}$ mice showed increased porosity of cortical bones. Whereas $Ank^{+/+}$ mice had most trabecular bone restricted to metaphyses, $Ank^{KI/KI}$ mice extended trabecular bones into diaphyses (Fig. 2F). Although significantly decreased trabeculation was observed in metaphyses of $Ank^{KI/KI}$ mice, the total volume of trabecular bone in femurs of $Ank^{+/+}$ and $Ank^{KI/KI}$ mice showed no significant difference. However, the structure model index (SMI) for $Ank^{KI/KI}$ mice suggested that trabecular bones are more rod-shaped in contrast to more plate-like in $Ank^{+/+}$ mice (Table 2). To our knowledge, distribution of trabecular bone in diaphyses of CMD patients has not been studied.

Skeletal phenotype of $Ank^{+/KI}$ mice

Heterozygous $Ank^{+/KI}$ mice were phenotypically similar to wildtype mice but exhibited a mild CMD-like phenotype as they aged. When comparing 1-yr-old $Ank^{+/+}$ ($n = 6$) and $Ank^{+/KI}$ ($n = 7$) male mice by μCT, we found that $Ank^{+/KI}$ mice developed a femoral shape comparable to $Ank^{KI/KI}$ mice with extensive trabecular bone in diaphyses (Fig. 2G). However, we did not detect a significant difference in hyperostotic phenotypes of craniofacial bones because of large variability (data not shown). Variable expressivity has been observed in autosomal dominant CMD patients as well.(29)

Biochemical analysis of $Ank^{KI/KI}$ mice

CMD patients present with elevated serum ALP, increased TRACP, and normal to slightly/transiently elevated PTH levels.(3,6,13,30) In sera of 10-wk-old fasted $Ank^{KI/KI}$ mice, we detected increases in ALP, a nonspecific bone marker, and TRACP5b, a marker of osteoclast numbers (Table 3). To further study osteoblast and osteoclast activities, we measured P1NP, a measure of bone formation, and CTX, a marker of osteoclast activity in age- and sex-matched samples from fasted animals. We detected a wide range of P1NP (60.5–137.15 ng/ml) and CTX (18.20–32.49 ng/ml) in $Ank^{+/+}$ mice. Most P1NP and CTX values in $Ank^{KI/KI}$ mice were in the upper end of these intervals or above, resulting in statistical significance (Table 3). These results, taken together, suggest increased bone turnover in $Ank^{KI/KI}$ mice.

Bone histology and histomorphometry of $Ank^{KI/KI}$ mice

We performed bone histology and histomorphometry on groups of 10-wk-old $Ank^{+/+}$ and $Ank^{KI/KI}$ male mice. Histology sections confirmed that $Ank^{KI/KI}$ calvariae were thicker than those of $Ank^{+/+}$ mice (Fig. 3A). $Ank^{KI/KI}$ femurs exhibited widened growth plates, reduced trabeculation in metaphyses, while retaining trabecular bone in diaphyses (Fig. 3B). Static histomorphometry showed that $Ank^{KI/KI}$ mice exhibited a small but significant increase in

TABLE 3. Serum Parameters in 10-wk-old $Ank^{+/+}$ and $Ank^{KI/KI}$ Male Mice

Serum levels	*Ank+/+*	$Ank^{KI/KI}$
ALP (μM/15ul) ($Ank^{+/+}$n = 6, $Ank^{KI/KI}$ *n* = 7)	17.16 ± 3.52	24.37 ± 5.78*
TRACP5b (U/liter) ($Ank^{+/+}$n = 7, $Ank^{KI/KI}$ *n* = 7)	7.15 ± 0.62	10.83 ± 1.89†
P1NP (ng/ml) ($Ank^{+/+}$n = 14, $Ank^{KI/KI}$ *n* = 14)	88.82 ± 25.24	108.57 ± 26.26*
CTX (ng/ml) ($Ank^{+/+}$n = 18, $Ank^{KI/KI}$ *n* = 18)	24.10 ± 4.49	30.49 ± 6.39†

Fasting serum was used for all measurement. Data are mean ± SD.
* $p < 0.05$.
† $p < 0.01$.

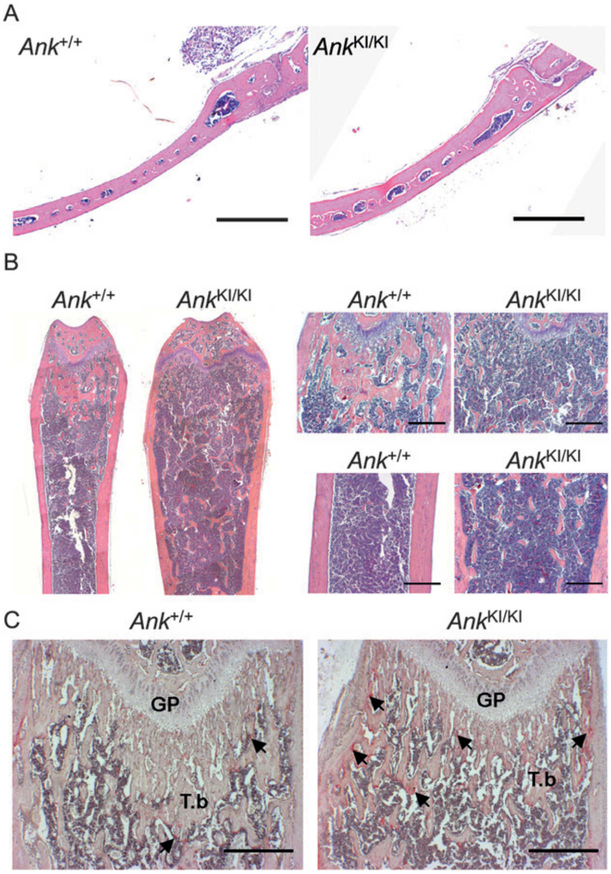

FIG. 3. Histology of $Ank^{+/+}$ and $Ank^{KI/KI}$ male mice. (A) Calvariae from 10-wk-old mice (H&E). (B) H&E staining of 10-wk-old mice: femurs (left panel), metaphyses (top right), and diaphyses (bottom right). (C) TRACP staining of femurs from 4-wk-old mice. Arrows indicate TRACP⁺ cells. GP, growth plate; T.b, trabecular bone. Scale bar = 500 μm.

TABLE 4. Static Histomorphometry of 10-wk-old $Ank^{+/+}$ and $Ank^{KI/KI}$ Male Mice

	$Ank^{+/+}$*(n = 5)*	$Ank^{KI/KI}$ *(n = 5)*
Calvariae		
Oc.Pm (mm)	0.44 ± 0.22	0.79 ± 0.07*
Oc.Pm/B.Pm (%)	10.15 ± 4.9	18.13 ± 4.51†
Femoral metaphyses	$Ank^{+/+}$ *(n = 8)*	$Ank^{KI/KI}$ *(n = 7)*
BVF (%)	9.2 ± 2.7	5.0 ± 2.2*
Trabecular thickness (μm)	33.1 ± 6.1	21.1 ± 4.5*
Ob.S/BS (%)	22.2 ± 2.7	25.4 ± 2.5†
Oc.S/BS (%)	3.4 ± 2	7.1 ± 2.5†
N.Oc/B.Pm (N/mm)	2.0 ± 1.1	4.1 ± 1.1*
N.Oc/T.Ar (N/mm²)	10.5 ± 5.7	20.8 ± 6.1*

Data are mean ± SD.
* $p < 0.01$.
† $p < 0.05$.
Oc.Pm, osteoclast surface; Oc.Pm/B.Pm, osteoclast surface measured on the total trabecular bone surface; Ob.S/BS, osteoblast surface (osteoblast surface/bone surface); Oc.S/BS, osteoclast surface (osteoclast surface/bone surface); N.Oc/B.Pm, osteoclast number over the total trabecular bone surface; N.Oc/T.Ar, number of osteoclasts normalized by total area measured.

osteoblast surface (1.15-fold) and osteoclast surface (2-fold) in femurs and an increase in osteoclast surface (1.8-fold) in calvariae (Table 4). Increased numbers of TRACP⁺ cells in the metaphysis, chondro-osseous junction, and the endosteum of femoral epiphysis and metaphysis were already observed in 1-mo-old $Ank^{KI/KI}$ mice (Fig. 3C).

For dynamic histomorphometry, we labeled mice with calcein and xylenol orange. $Ank^{KI/KI}$ mice showed a decreasing trend in mineral apposition rate in femoral metaphyses ($Ank^{+/+}$: 1.83 ± 0.24 μm/d, *n* = 6; $Ank^{KI/KI}$: 1.63 ± 0.08 μm/d, *n* = 10; *p* = 0.1) and calvariae ($Ank^{+/+}$: 1.34 ± 0.28 μm/d, *n* = 7; $Ank^{KI/KI}$: 1.07 ± 0.25 μm/d, *n* = 9; *p* = 0.06). However, no significant difference in bone formation rate of $Ank^{+/+}$ and $Ank^{KI/KI}$ littermates was observed in femoral metaphyses ($Ank^{+/+}$: 0.66 ± 0.18 μm³/μm²/d; $Ank^{KI/KI}$: 0.64 ± 0.16 μm³/μm²/d; *p* = 0.82) or in calvariae ($Ank^{+/+}$: 0.547 ± 0.239 μm³/μm²/d; $Ank^{KI/KI}$: 0.529 ± 0.257 μm³/μm²/d; *p* = 0.88).

In vitro osteoclastogenesis

Yamamoto et al.[13] described dysfunctional osteoclastogenesis in bone marrow–derived cultures of a 3-yr-old CMD patient who had increased serum TRACP and elevated urinary hydroxyproline excretion. We examined osteoclastogenesis using $Ank^{+/+}$ and $Ank^{KI/KI}$ bone marrow–derived macrophage (BMM) cultures. BMMs were cultured in the presence of M-CSF and RANKL for 4, 5, 6, and 7 days. Cells were TRACP stained, and TRACP⁺ cells with three or more nuclei were considered osteoclasts. During in vitro osteoclast differentiation, $Ank^{KI/KI}$ BMMs formed significantly fewer and smaller osteoclasts (Fig. 4A). Furthermore, $Ank^{KI/KI}$ cells showed marked reduction of mineral resorption on calcium phosphate–coated slides (Fig. 4A). This result was confirmed by resorption pit assays on bone chips (Fig. 4B; $Ank^{+/+}$ = 41.6 ± 5.83%, $Ank^{KI/KI}$ = 17.6 ± 3.10%, $p < 0.01$). $Ank^{+/KI}$ BMMs showed significant decreased osteoclast formation and resorption,

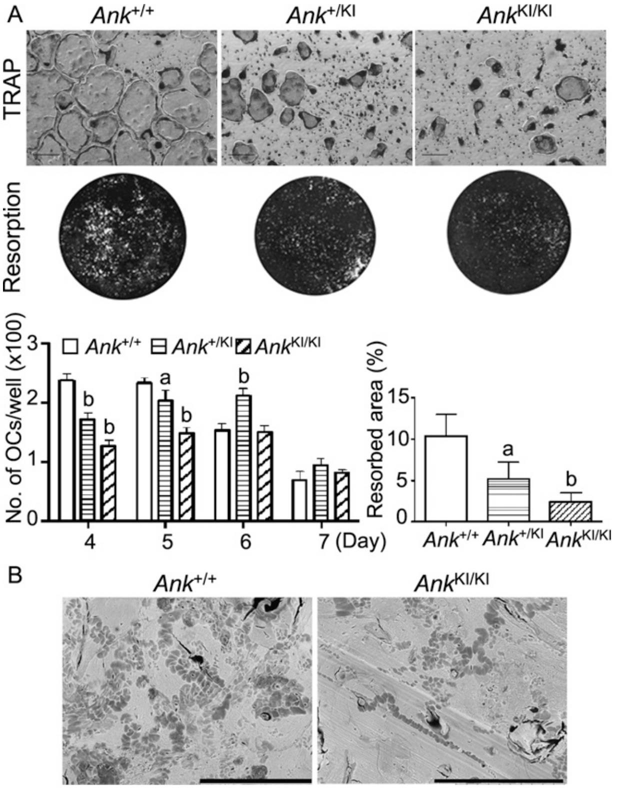

FIG. 4. In vitro osteoclast assays. (A) Representative images of TRACP staining at day 5 and of resorption of osteologic slides in BMM cultures. Histograms show number of mature osteoclasts per well and percentile of the resorbed area., Analysis of TRACP staining was performed by two-way ANOVA followed by Bonferroni test compared with the *Ank*$^{+/+}$ group for each time point. Resorption assay was evaluated by one-way ANOVA with Tukey's multiple-comparison test. $^{a}p < 0.05$; $^{b}p < 0.01$. Scale bar = 200 μm. (B) Representative images of resorption pit assay on bone chips. Scale bar = 300 μm.

although less severe than *Ank*$^{KI/KI}$ cultures. We conclude that the Ank Phe377del mutation leads to decreased in vitro osteoclastogenesis, consistent with the finding in a CMD case report.(13)

Bone matrix analysis of Ank$^{KI/KI}$ mice

To evaluate the effects of the *Ank* mutation on bone quality, we examined bone matrix on femoral sections by FTIR analysis. Mineral content (mineral-to-matrix ratio), which corresponds to ash weight of bone, was significantly decreased in the central cortical bone of *Ank*$^{KI/KI}$ femurs (Fig. 5A). Collagen maturity, which is determined by the relative ratio of nonreducible and reducible collagen cross-links, was significantly reduced in *Ank*$^{KI/KI}$ mice compared with *Ank*$^{+/+}$ mice (Fig. 5A). The carbonate-to-phosphate ratio (replacement of phosphate by carbonate groups) and crystallinity (which corresponds to the crystal size and perfection determined by X-ray diffraction) remained unaffected in cortical bones of *Ank*$^{KI/KI}$ mice (Fig. 5A).

To determine the size and type of crystals, we used wide-angle X-ray diffraction. In agreement with FTIR results, crystal size and perfection in bone powder from tibia and scapula were comparable between *Ank*$^{+/+}$ and *Ank*$^{KI/KI}$ mice (Fig. 5B). Furthermore, we detected hydroxyapatite, not CPPD, crystals in both groups (Fig. 5C).

Comparison of skeletal phenotypes of Ank$^{KI/KI}$ and Ank$^{ank/ank}$ mice

We compared joint and bone phenotypes of *Ank*$^{KI/KI}$ and *Ank*$^{ank/ank}$ mice. Both *Ank*$^{KI/KI}$ and *Ank*$^{ank/ank}$ mice developed joint stiffness and could not grab cage bars starting at ages of 4–5 wk. In *Ank*$^{ank/ank}$ joints, we observed excessive bony deposits, which appeared more severe than in *Ank*$^{KI/KI}$ mice (Fig. 6A). *Ank*$^{ank/ank}$ mice developed less trabeculation in metaphyses; however, in contrast to *Ank*$^{KI/KI}$ mice, they failed to present mandibular hyperostosis, narrowed nasal sinuses, flared metaphyses, or trabecular bone in diaphyses (Figs. 6B and 6C). Those findings suggest that the CMD-like phenotype in *Ank*$^{KI/KI}$ mice is distinct and is not simply caused by a loss of PPi transport function of ANK.

DISCUSSION

Although *Ank*$^{KI/KI}$ mice exhibit many features of CMD, they differ from human CMD in two aspects. Whereas the Phe377del mutation in humans leads to CMD in an AD trait, most heterozygous mice appear phenotypically closer to wildtype littermates but develop an intermediate phenotype with variable expressivity as they age. It is not unusual that the expression of an AD human disease gene results in severe phenotypes only in homozygote mice.(31–33) Differences between the disease characteristics of autosomal dominant CMD in humans and *Ank*$^{+/KI}$ mice may be because of species-specific phenotypic thresholds and lifespan. Joint stiffness of elbows, knees, paws, and vertebrae in *Ank*$^{KI/KI}$, *Ank*$^{ank/ank}$, and *Ank*$^{null/null}$ mice has not been reported in CMD patients. However, we have not found patients who are homozygous or compound heterozygous for CMD mutations.

Ank$^{ank/ank}$ mice display more severe ectopic mineralization in joints and lack certain CMD-specific features in comparison with *Ank*$^{KI/KI}$ mice. The joint phenotype in *Ank* loss-of-function models is caused by ectopic deposition of HA from reduced extracellular PPi, which is an inhibitor of mineralization. It is conceivable that the CMD mutation does not fully inhibit PPi transport or that extracellular PPi synthesis by phosphodiesterases in *Ank*$^{KI/KI}$ mice is higher than in *Ank*$^{ank/ank}$ or *Ank*$^{null/null}$ mice. The unique CMD-like phenotype develops before the onset of joint stiffness in *Ank*$^{KI/KI}$ mice. In 1-wk-old *Ank*$^{KI/KI}$ mice, we observed a massive mandible, flaring metaphyses, and less trabecular bone but more trabeculation in diaphyses (data not shown). These skeletal comparisons suggest that *Ank*$^{KI/KI}$ mice represent a better model for CMD and loss of PPi transporter function is not the sole cause for CMD. Based on the clustering of CMD mutations, we hypothesize that mutant ANK potentially alters protein–protein interactions and/or intracellular signal transduction, resulting in the unique CMD phenotype.

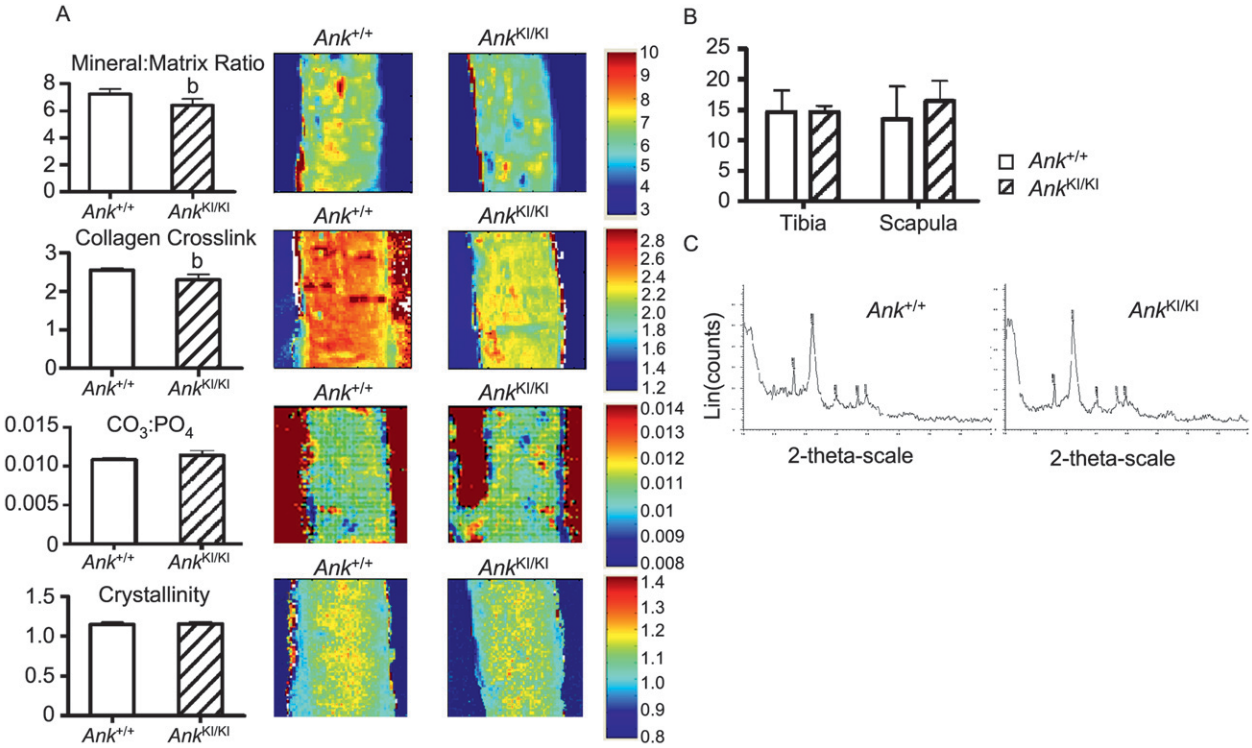

FIG. 5. FTIR and X-ray diffraction analysis of bones from 10-wk-old *Ank*$^{+/+}$ and *Ank*$^{KI/KI}$ male mice. (A) Mineral:matrix ratio; collagen cross-linking; carbonate:phosphate ratio; crystallinity of central cortical bones from 10-wk-old *Ank*$^{+/+}$ and *Ank*$^{KI/KI}$ femurs. Numerical scales represent the range of intensity ratios applied for each parameter. Histograms for individual images are shown on the left. (B) Analysis of crystal size in bone powder from tibias and scapulae by X-ray diffraction. (C) Crystalline phases in bone powder identified by wide-angle X-ray diffraction. Data are mean ± SD. Statistical significance by Student's *t*-test ($^{b}p < 0.01$).

Biochemical serum markers can be used as measures for osteoblast and osteoclast activities.(34) Total serum ALP is widely used as a marker for bone metabolism, although it is not bone specific. Data from two of our CMD patients showed elevated levels for both bone- and liver-specific ALP (data not shown). Increased TRACP5b is consistent with increased osteoclast numbers as shown by static histomorphometry in *Ank*$^{KI/KI}$ mice. Serum levels of P1NP and CTX, measures of bone formation and bone resorption, have not been reported in CMD patients. We interpret the increased serum P1NP and CTX in *Ank*$^{KI/KI}$ mice as increased bone turnover. Decreased trabecular thickness and increased cortical porosity in these mice may be results of increased bone remodeling activity.

We observed hypomineralized bone matrix in *Ank*$^{KI/KI}$ mice by ash weight, μCT, and FTIR. Reduced BMD has also been reported in one CMD patient.(1) Conversely, DXA showed increased BMC in skulls, mandibles, and femurs of *Ank*$^{KI/KI}$ mice. Although DXA is a clinically used noninvasive method to assess bone mass, it only measures density per area and not by volume. Hyperostosis and changes in bone shape could result in overestimation of BMC and BMD and should be taken into consideration when using DXA.(35) We suggest that hyperostosis cannot be equated with sclerosis as is done in some clinical reports of CMD.

FTIR analysis provides information about chemical properties of bone. The mineral phase in the femoral cortex was homogeneously distributed; however, the mineral to matrix ratio and collagen maturity were decreased in *Ank*$^{KI/KI}$ specimen. Mineralization defects can be caused by improper collagen cross-links, enhanced bone matrix synthesis, or inappropriate mineralization of the secreted matrix.(36) Overall bone strength can be attributed to both structural and material components. Therefore, it is possible that increased bone diameters with club shape and abnormal distribution of trabecular bones in diaphyses is an attempt to compensate for poor bone quality and provide improved structural properties in *Ank*$^{KI/KI}$ mice.

A tight balance between the levels of extracellular phosphate (Pi) and pyrophosphate (PPi) is required to control mineralization. Extracellular PPi (ePPi) acts as a potent inhibitor of HA mineralization and exhibits a bimodal effect on crystal formation. Low ePPi leads to excess HA formation, whereas supersaturation of ePPi promotes CPPD crystal deposition.(37) Whether mutant ANK causes altered PPi transport into extracellular matrix has not been tested in CMD patients. However, an in vitro assay showed that overexpression of a BAC-*Ank*^{G389R} construct, one of the identified CMD-causing mutations, in oocytes leads to significantly reduced PPi uptake.(25) We determined by X-ray diffraction that abnormal mineral crystals from bones of *Ank*$^{KI/KI}$ mice consist of HA and not CPPD, which indicated that *Ank*$^{KI/KI}$ mice do not exhibit excessive ePPi levels. Whether the Phe377del mutation in ANK results in less PPi transport to extracellular matrix and whether other PPi regulators, such as ectonucleotide

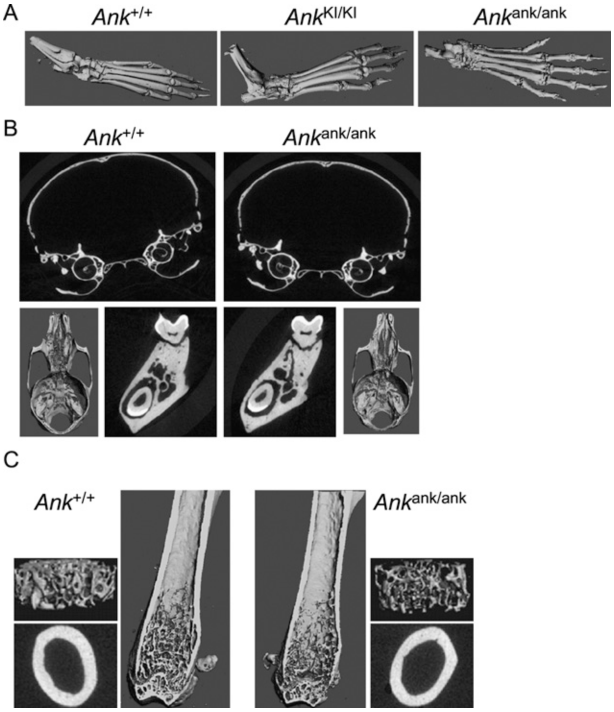

FIG. 6. Skeletal phenotype of 3-mo-old *Ank*$^{\mathrm{ank/ank}}$ male mice. (A) 3D μCT images comparing hind feet of *Ank*$^{+/+}$, *Ank*$^{\mathrm{KI/KI}}$, and *Ank*$^{\mathrm{ank/ank}}$ animals. (B) μCT images of skulls, cranial and nasal cavities, and mandibles. (C) Internal view of *Ank*$^{+/+}$ and *Ank*$^{\mathrm{ank/ank}}$ femurs. 3D reconstructions of trabeculation in metaphysis and cross-sectional slices of cortical bone in diaphysis.

pyrophosphatase phosphodiesterases or tissue-nonspecific ALP, can compensate for a decrease of ANK activity in this mouse model is a subject of future studies.

To date, two hypotheses have been proposed for the pathogenesis of CMD: reduced bone resorption(12,13) and increased bone formation secondary to increased bone turnover.(3) Both hypotheses, however, cannot fully explain hyperostosis of craniofacial bones and undertrabeculated metaphyses of long bones in CMD. A previous study and our data showed decreased osteoclastogenesis in vitro, whereas elevated serum TRACP5b was detected in a CMD patient(13) and in *Ank*$^{\mathrm{KI/KI}}$ mice. Therefore, increased cell numbers could possibly be a compensation of reduced osteoclast function in CMD patients and *Ank*$^{\mathrm{KI/KI}}$ mice. Our results suggested that *Ank*$^{\mathrm{KI/KI}}$ mice have increased bone turnover, which may lead to either increased or decreased bone mass. We propose that metaphyses in *Ank*$^{\mathrm{KI/KI}}$ mice develop imbalanced bone remodeling in favor of resorption, whereas in cranial bones, bone formation overweighs bone resorption. Cranial vault and jawbones are formed by intramembranous ossification, whereas long bones develop through endochondral bone formation, a process involving chondrogenesis.(38,39) Calcified cartilage septa are required for osteoblasts to lay down primary trabecular bone.(40) Because *Ank* is expressed in chondrocytes, it is possible that a primary chondrocyte defect contributes to the long bone phenotype. The increase in osteoclast numbers, the proximity to the growth plate, and an environment rich in bone marrow (a source of osteoclast progenitors) may result in net bone loss in the metaphysis. Transverse widening of long bone growth plates is regulated by appositional growth at the groove of Ranvier.(41,42) Bone bark, a component of the groove of Ranvier, is responsible for widening of the cortical portion of bone, and endosteal and periosteal osteoclast activity in this region is needed for contouring bone shape and width.(42) The abnormal metaphyseal bone shape may be a result of increased endosteal bone resorption in the region described as bone bark and of reduced periosteal resorption outside of the conductive metaphyseal environment. On the other hand, in craniofacial bones, there is less bone marrow present and, despite increased numbers of osteoclasts, their overall activity may be reduced.

In summary, we successfully generated the first mouse model for CMD, which will allow the study of CMD pathogenesis at cellular and molecular levels. Our results imply a previously unappreciated complexity of the CMD phenotype involving both osteoblasts and osteoclasts. We expect that additional studies of this model will help to address the mechanisms of CMD-causing *ANK* mutations and potentially lead to therapeutic approaches for CMD.

ACKNOWLEDGMENTS

We are indebted to members of the UCHC Bone Group at UCHC for helpful discussions. The authors thank the μCT and Histomorphometry facilities at UCHC for support. The project was supported by Grants AR49539 (NIAMS) to E.J.R. and DE007302 to C.J.W.

REFERENCES

1. Elcioglu N, Hall CM 1998 Temporal aspects in craniometaphyseal dysplasia: Autosomal recessive type. Am J Med Genet **76:**245–251.
2. Ramseyer LT, Leonard JC, Stacy TM 1993 Bone scan findings in craniometaphyseal dysplasia. Clin Nucl Med **18:**137–139.
3. Fanconi S, Fischer JA, Wieland P, Giedion A, Boltshauser E, Olah AJ, Landolt AM, Prader A 1988 Craniometaphyseal dysplasia with increased bone turnover and secondary hyperparathyroidism: Therapeutic effect of calcitonin. J Pediatr **112:**587–591.
4. Haverkamp F, Emons D, Straehler-Pohl HJ, Zerres K 1996 Craniometaphyseal dysplasia as a rare cause of a severe neonatal nasal obstruction. Int J Pediatr Otorhinolaryngol **34:**159–164.
5. Key LL Jr, Volberg F, Baron R, Anast CS 1988 Treatment of craniometaphyseal dysplasia with calcitriol. J Pediatr **112:**583–587.
6. Cheung VG, Boechat MI, Barrett CT 1997 Bilateral choanal narrowing as a presentation of craniometaphyseal dysplasia. J Perinatol **17:**241–243.
7. Schwahn B, Schaper J, Herkenrath P, Michel O, Schoenau E 1996 Autosomal-dominante kraniometaphysaere dysplasie. Monatsschr Kinderheilkd **144:**1073–1077.
8. Langer LO Jr, Brill PW, Afshani E, Williams CA, Thomas IT, Frias JL 1991 Radiographic features of craniometadiaphyseal dysplasia, wormian bone type. Skeletal Radiol **20:**37–41.
9. Richards A, Brain C, Dillon MJ, Bailey CM 1996 Craniometaphyseal and craniodiaphyseal dysplasia, head and neck manifestations and management. J Laryngol Otol **110:**328–338.

10. Halliday J 1949 A rare case of bone dystrophy. Br J Surg **37:**52–63.
11. Jackson WPU, Albright F, Drewery G, Hanelin J, Rubin ML 1954 Metaphyseal dysplasia, epiphyseal dysplasia, diaphyseal dysplasia and related conditions. Arch Intern Med **94:**871–885.
12. Millard DR Jr, Maisels DO, Batstone JH, Yates BW 1967 Craniofacial surgery in craniometaphyseal dysplasia. Am J Surg **113:**615–621.
13. Yamamoto T, Kurihara N, Yamaoka K, Ozono K, Okada M, Yamamoto K, Matsumoto S, Michigami T, Ono J, Okada S 1993 Bone marrow-derived osteoclast-like cells from a patient with craniometaphyseal dysplasia lack expression of osteoclast-reactive vacuolar proton pump. J Clin Invest **91:**362–367.
14. Gorlin RJ, Anderson RC, Blaw M 1969 Multiple lentigenes syndrome. Am J Dis Child **117:**652–662.
15. Reichenberger E, Tiziani V, Watanabe S, Park L, Ueki Y, Santanna C, Baur ST, Shiang R, Grange DK, Beighton P, Gardner J, Hamersma H, Sellars S, Ramesar R, Lidral AC, Sommer A, Raposo do Amaral CM, Gorlin RJ, Mulliken JB, Olsen BR 2001 Autosomal dominant craniometaphyseal dysplasia is caused by mutations in the transmembrane protein ANK. Am J Hum Genet **68:**1321–1326.
16. Nurnberg P, Thiele H, Chandler D, Hohne W, Cunningham ML, Ritter H, Leschik G, Uhlmann K, Mischung C, Harrop K, Goldblatt J, Borochowitz ZU, Kotzot D, Westermann F, Mundlos S, Braun HS, Laing N, Tinschert S 2001 Heterozygous mutations in ANKH, the human ortholog of the mouse progressive ankylosis gene, result in craniometaphyseal dysplasia. Nat Genet **28:**37–41.
17. Pendleton A, Johnson MD, Hughes A, Gurley KA, Ho AM, Doherty M, Dixey J, Gillet P, Loeuille D, McGrath R, Reginato A, Shiang R, Wright G, Netter P, Williams C, Kingsley DM 2002 Mutations in ANKH cause chondrocalcinosis. Am J Hum Genet **71:**933–940.
18. Williams CJ, Zhang Y, Timms A, Bonavita G, Caeiro F, Broxholme J, Cuthbertson J, Jones Y, Marchegiani R, Reginato A, Russell RG, Wordsworth BP, Carr AJ, Brown MA 2002 Autosomal dominant familial calcium pyrophosphate dihydrate deposition disease is caused by mutation in the transmembrane protein ANKH. Am J Hum Genet **71:**985–991.
19. Zaka R, Stokes D, Dion AS, Kusnierz A, Han F, Williams CJ 2006 P5L mutation in Ank results in an increase in extracellular inorganic pyrophosphate during proliferation and nonmineralizing hypertrophy in stably transduced ATDC5 cells. Arthritis Res Ther **8:**R164.
20. Ho AM, Johnson MD, Kingsley DM 2000 Role of the mouse ank gene in control of tissue calcification and arthritis. Science **289:**265–270.
21. Carr G, Sayer JA, Simmons NL 2007 Expression and localisation of the pyrophosphate transporter, ANK, in murine kidney cells. Cell Physiol Biochem **20:**507–516.
22. Gurley KA, Chen H, Guenther C, Nguyen ET, Rountree RB, Schoor M, Kingsley DM 2006 Mineral formation in joints caused by complete or joint-specific loss of ANK function. J Bone Miner Res **21:**1238–1247.
23. Sweet HO, Green MC 1981 Progressive ankylosis, a new skeletal mutation in the mouse. J Hered **72:**87–93.
24. Hakim FT, Cranley R, Brown KS, Eanes ED, Harne L, Oppenheim JJ 1984 Hereditary joint disorder in progressive ankylosis (ank/ank) mice. I. Association of calcium hydroxyapatite deposition with inflammatory arthropathy. Arthritis Rheum **27:**1411–1420.
25. Gurley KA, Reimer RJ, Kingsley DM 2006 Biochemical and genetic analysis of ANK in arthritis and bone disease. Am J Hum Genet **79:**1017–1029.
26. Hausamen TUH, R. Rick, W Gross, W 1967 Optimal conditions for the determination of serum alkaline phosphatase by a new kinetic method. Clin Chim Acta **15:**241–245.
27. Parfitt AM, Drezner MK, Glorieux FH, Kanis JA, Malluche H, Meunier PJ, Ott SM, Recker RR 1987 Bone histomorphometry: Standardization of nomenclature, symbols, and units. Report of the ASBMR Histomorphometry Nomenclature Committee. J Bone Miner Res **2:**595–610.
28. Gorlin RJ, Cohen MM Jr, Hennekam RCM 2001 Syndromes of the Head and Neck, 4th ed. Oxford Press, New York, NY, USA.
29. Carnevale A, Grether P, del Castillo V, Takenaga R, Orzechowski A 1983 Autosomal dominant craniometaphyseal dysplasia. Clinical variability. Clin Genet **23:**17–22.
30. Sheppard WM, Shprintzen RJ, Tatum SA, Woods CI 2003 Craniometaphyseal dysplasia: A case report and review of medical and surgical management. Int J Pediatr Otorhinolaryngol **67:**71–77.
31. Chipman SD, Sweet HO, McBride DJ Jr, Davisson MT, Marks SC Jr, Shuldiner AR, Wenstrup RJ, Rowe DW, Shapiro JR 1993 Defective pro alpha 2(I) collagen synthesis in a recessive mutation in mice: A model of human osteogenesis imperfecta. Proc Natl Acad Sci USA **90:**1701–1705.
32. Ueki Y, Lin CY, Senoo M, Ebihara T, Agata N, Onji M, Saheki Y, Kawai T, Mukherjee PM, Reichenberger E, Olsen BR 2007 Increased myeloid cell responses to M-CSF and RANKL cause bone loss and inflammation in SH3BP2 ''cherubism'' mice. Cell **128:**71–83.
33. Liao BY, Zhang J 2008 Null mutations in human and mouse orthologs frequently result in different phenotypes. Proc Natl Acad Sci USA **105:**6987–6992.
34. Seibel MJ 2000 Molecular markers of bone turnover: Biochemical, technical and analytical aspects. Osteoporos Int **11**(Suppl 6)**:**S18–S29.
35. Ott SM, O'Hanlan M, Lipkin EW, Newell-Morris L 1997 Evaluation of vertebral volumetric vs. areal bone mineral density during growth. Bone **20:**553–556.
36. Knott L, Bailey AJ 1998 Collagen cross-links in mineralizing tissues: A review of their chemistry, function, and clinical relevance. Bone **22:**181–187.
37. Johnson K, Terkeltaub R 2005 Inorganic pyrophosphate (PPI) in pathologic calcification of articular cartilage. Front Biosci **10:**988–997.
38. Karsenty G 1999 The genetic transformation of bone biology. Genes Dev **13:**3037–3051.
39. Olsen BR, Reginato AM, Wang W 2000 Bone development. Annu Rev Cell Dev Biol **16:**191–220.
40. Fazzalari NL, Moore AJ, Byers S, Byard RW 1997 Quantitative analysis of trabecular morphogenesis in the human costochondral junction during the postnatal period in normal subjects. Anat Rec **248:**1–12.
41. Shapiro F, Holtrop ME, Glimcher MJ 1977 Organization and cellular biology of the perichondrial ossification groove of ranvier: A morphological study in rabbits. J Bone Joint Surg Am **59:**703–723.
42. Schollmeier G, Uhthoff HK, Lewandrowski KU, Fukuhara K 1999 Role of bone bark during growth in width of tubular bones. A study in human fetuses. Clin Orthop Relat Res 291–299.

Received in original form August 3, 2008; revised form January 14, 2009; accepted February 11, 2009.